# Moisture Migration Characterization of Bitumen Emulsion-based Cold In-place Recycling Mixture over Curing

Jiwang Jiang[1,*], Zili Zhao[1], Xi Jiang[2], Zhen Leng[2,*], Bin Yang[2], Fujian Ni[1]

[1] School of Transportation, Southeast University, Nanjing, Jiangsu, China, 211189

[2] Department of Civil and Environmental Engineering, the Hong Kong Polytechnic University, Kowloon 999077, Hong Kong

[*] Corresponding author. Email: jiang_jiwang@seu.edu.cn (J. Jiang); zhen.leng@polyu.edu.hk (Z Leng).

## Abstract

Bitumen Emulsion-based Cold In-place Recycling (BE-CIR) pavement has been widely used all around the world due to its superior environmental benefits. BE-CIR pavement presents a unique moisture migration behavior after compaction because of the breaking of bitumen emulsion, contributing to the strength formation of the mixture. However, previous studies have mainly evaluated water diffusion by mass loss and ignored its effect in the depth direction. In this study, a one-way evaporation method was developed to simulate the field moisture migration of the BE-CIR mixture specimens. An image processing method was proposed to extract the moisture distribution of the BE-CIR mixtures by images from Multiple X-ray Computed Tomography (XCT) scanning tests at different curing times. The effects of curing temperature were investigated as well. According to the detailed description of the micro-morphology variation of moisture instead of only mass loss, a gradient feature in the depth direction which was more significant near the surface in contact with air could be found. Among different curing stages, the gradient characteristic could be observed only at the curing ages of 3 to 7d, and moisture was more likely to migrate from the edges and have a more irregular thickness at the curing of 0 to 3d. Curing temperature would significantly influence the range of gradients and the variation of water content in the depth direction. The outcomes of this study can enhance the understanding of the dynamic moisture migration characteristics of the BE-CIR pavement over curing.

**Keywords:** Cold-in-place recycling, Moisture movement, XCT scanning test, Image Processing, Water film thickness.

## 1 Introduction

Depletion of natural resources necessitates the adoption of recycling as a rehabilitation technology in pavement engineering. Reclaimed asphalt pavement (RAP) material is obtained by milling damaged pavements or from full-depth removal of asphalt pavements [1]. Among different RAP recycling technologies, the Cold In-place Recycling (CIR) pavement is one of the most sustainable techniques that enables 100% reuse of the RAP without the need for heating and transportation [2, 3]. In recent years, it has gained worldwide popularity as a cost-effective and environmental-friendly pavement rehabilitation strategy in many countries[4, 5]. Many attractive features can also be reached, including repairing pavement defects, extending the longevity of asphalt pavements, reducing landfill disposal pressure and improving riding comfort [6].

Bitumen emulsions or foamed bitumen are commonly used as binders for CIR. These two types of bitumen present a significantly lower viscosity than conventional bitumen and appear as a liquid at ambient temperatures, therefore allowing CIR mixtures to be mixed and compacted at lower temperatures. Bitumen emulsion, which is a dispersion of small charged bitumen droplets suspended in water under the effect of emulsifiers, plays an important role in the workability, curing behavior, and mechanical performance of the BE-CIR mixture. For the purpose of CIR, slow-setting and medium-setting emulsions are more commonly used since they allow for more mixing time and extended workability [7]. In addition to bitumen, some inorganic additives, such as Portland cement, are often used to improve the mechanical properties of CIR mixtures. By adding Portland cement, it can have the effect of promoting the dispersion of the bitumen, regulating the breaking of the emulsion and accelerating the curing time. [8-10]. In order to promote the uniform coating of the bitumen emulsion and enhance the packing of RAP aggregates, extra water should be added based on the field environmental conditions in the mixing process [11, 12]. Therefore, mechanical performance of BE-CIR mixture is a joint reflection of properties for the bitumen emulsion and cement[13, 14]. Depending on the bitumen to cement ratio, commonly expressed as b/c, the bitumen emulsion-cement composite system can show widely different microstructures that manifest widely different mechanical behaviour[15, 16]. As the b/c value changes from large to small, the microstructure changes from bitumen-dominated to the cement-dominated, resulting in a transition in mechanical properties from a viscous to an elastic material[17-19].

Due to the hydration of cement and the demulsification of asphalt emulsion, the mechanical properties of BE-CIR depend significantly on the curing time and conditions[20-22]. The curing process is accompanied by water-related phenomena including exudation, evaporation, suction, emulsion breaking and cement hydration, which finally lead to a reduction of moisture and an increase in stiffness and strength [23-25]. Therefore, it is essential to investigate the moisture variation of the BE-CIR mixture during curing process. Many studies have attempted to directly measure moisture changes in the field based on installed humidity and temperature sensors in the CIR pavement to measure the water content and temperature of the BE-CIR mixtures over curing[26-28]. The University of Iowa (US) research group [28] installed sensors at about mid-depth of the CIR layers in several CIR projects with foamed bitumen or emulsified bitumen to optimize the timing for overlay. It is concluded that the moisture content measured by the sensors showed a project-dependent values and significantly affected by the bitumen type. Cox et al. [26] investigated both the moisture content during compaction and curing and concluded that there is a quick reduction in the water content during compaction, while the evolution of water content during the 14 days of curing fluctuated with the environment.

Despite the valuable guidance from field studies, field results are hardly obtained and not reproducible due to the complexity of sensor emplacement and the volatility and randomness the outdoor environment. More indoor studies have been carried out to investigate the water migration behaviour through controlled curing conditions[29-31]. Saadoon et al. [32, 33] studied the moisture evaporation of CIR mixtures with different cement fillers. They found that the Marshall stability had a good relation with the water loss process which is mainly influenced by the asphalt emulsion but not the type and quantity of cement. Thus, the drying process of bitumen emulsion and its influencing factors have been further studied. The drying theory of emulsion was usually used to quantified the process of water reduction in the bitumen emulsion[34-36]. Moreover, the mesoscale model such as mortar has also been investigated to establish the interphase relations with the corresponding mixture[15, 37-39]. The assessment of water migration behavior in most studies is mainly based on the mass change of samples during curing[31, 40, 41], custom-made electrode method has also been used[42]. However, the evaluation of moisture by these methods is only obtained from the change in moisture content, and there is a lack of more detailed moisture distribution parameters to better understand the moisture migration behavior during curing. In addition, the BE-CIR layer is viewed as an integrated whole during curing in most cases, and moisture fluctuation in the depth direction during curing is ignored. To address this problem, Zhao et al. [43] investigated the field moisture condition of BE-CIR pavement at different depths by humidity and temperature sensors and they found that the field moisture evaporation of the BE-CIR pavement presents gradient characteristics. Although the moisture migration with depth may significantly affected by the compaction energy of the road roller in the field, it is also worth considering in the laboratory due to the evaporation and this characterization is difficult to obtain only by the change of mass.

To this end, it is important to further characterize the behaviour of moisture within the BE-CIR mixture over curing process considering the depth direction. Therefore, the main objectives of this research are a) develop a specified image-based method to identify and extract the micro-structure of water film within BE-CIR mixture over curing; b) characterize the migration process of moisture in depth direction of BE-CIR mixture during curing by newly proposed micro-morphology parameters; c) explore the effects of curing temperature on the moisture migration of BE-CIR mixture.

## 2 Mix Preparation and Test Program

### 2.1 Materials and mixture design

A BE-CIR project of Fenguan Highway (G15) in Jiangsu Province of China was the basement of this study. The materials and mixture design were consistent with the project[43]. In this project, the original 10 cm surface course were 100% recycled into a BE-CIR layer, and then a 5 cm overlay was placed on top of the BE-CIR layer. Therefore, the laboratory samples were prepared by pure RAP, and the gradation of RAP material from this project fell within the medium gradation limitations specified by the Jiangsu Province agency [44] as presented in Figure 1. The Portland cement (PO. 42.5) was determined to be the inorganic additive with a content of 2.2 wt% base on the project. The property of emulsified bitumen was selected as cationic slow-setting, and the optimum content was determined to be 3.3 wt% with satisfactory Marshal Stability and Indirect Tensile Strength. The basic information of bitumen emulsion are shown in Table 1. The content of the extra water was calculated by the total moisture content minus the moisture in the emulsified bitumen. The maximum dry density method [45] was used for determining the optimal total moisture content. Finally, the optimal total moisture content was determined to be 4.0 wt%, and the content of extra water was calculated to be 2.8 wt% by subtracting the water in the emulsified asphalt from the total moisture content.

Table 1 Properties of emulsified bitumen

| Characteristics of the emulsified bitumen | |
|---|---|
| Residue content by evaporation (%) | 64 |
| Penetration (25 °C; 0.1 mm) | 59.1 |
| softening point (◦C) | 59.9 |
| Ductility (15 °C; cm) | 110 |

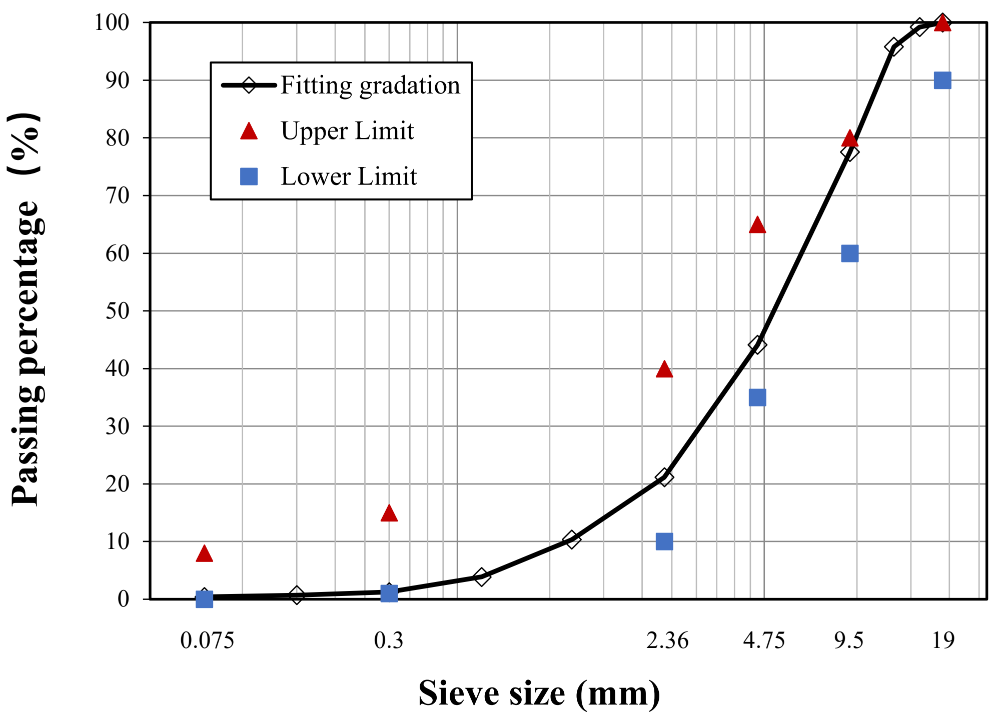


Figure 1 Aggregate gradation of BE-CIR mixtures.

## 2.2 Compaction and curing condition

The laboratory BE-CIR mixtures were fabricated by the Superpave gyratory compaction (SGC) method with a diameter of 100 mm and a height of 100 mm. The production process of BE-CIR mixtures was initially adding the cement to the RAP and mixing with extra water for one minute, then the emulsified bitumen was added and mixed for another four minutes. The gyratory number was set as 30 for all specimens to ensure that the compaction energy of all samples was the same. The number of gyratory gyrations for the compaction was determined to achieve the target air void of 10% which was consisted with the mix design of the in-situ BE-CIR project[43].

The compacted BE-CIR specimens usually were cured in the oven unsealed at a specified constant temperature. This curing method was widely used due to its simplicity and time-saving. However, it considers the BE-CIR specimen as an integrated whole but ignores the gradient moisture migration characteristics under the boundary condition in the field environment. This research focuses on the moisture migration behavior during curing, a semi-sealed laboratory curing condition was designed to simulate the in-suit moisture migration process. A tarp made of Teflon as a waterproofing layer was covered around the side and bottom surfaces of the specimens (Figure 2) to ensure moisture inside the mixture can only evaporate from the upper surface.

Curing temperature affecting water evaporation is considered in this paper. As shown in Table 2, BE-CIR1 represents the initial moisture content of 4% and curing in the oven at 40°C, which is similar to the field project. BE-CIR2 has a lower curing temperature of 25°C to simulate projects constructed in autumn or winter. Three parallel specimens of each BE-CIR were fabricated for the following tests.

Table 2 Controlled variable of different mixture

| Mix ID | initial moisture content (%) | curing temperature (°C) |
|---|---|---|
| BE-CIR1 | 4 | 40 |
| BE-CIR2 | 4 | 25 |

## 2.3 Experimental program

Figure 2 illustrates the overall process of the test. The duration of the XCT scanning test is taken into account during the fabrication as the XCT scanning test would take approximately 2-3 hours per specimen. Therefore, each specimen was compacted every 3 hours to ensure the same curing time when it was scanned. XCT scanning test was conducted for each sample immediately after compaction and these results were recorded as time 0. It is important to note that as the moisture migration behavior is more pronounced in the early time of curing, changes in moisture during

XCT scanning test need to be minimized. As the experiments in this research were conducted in the local winter, the ambient outdoor temperature was approximately 5 °C. The samples were fabricated indoors at a temperature of 30 °C, then immediately placed outdoors for wrapping waterproofing layer. and finally sent to the XCT chamber for testing. According to testing the mass between before and after the XCT scan test, the difference was only 1-2 g. Therefore, it can be assumed that the result is almost the same with that after compaction. In subsequent studies, it is suggested that researchers can reduce the effect of the XCT scanning test process during early curing time by controlling the ambient temperature.

Then, the samples were placed in the oven at the corresponding constant temperature for curing. According to a previous in-situ monitoring study, the change in humidity index (*HI*) presents two obvious stages of a rapid decline in the first 3 days and a continuous dropping in the next curing period[43]. The first stage is the HI drops rapidly lasting approximately 3 days, and in the second stage, HI decreases slowly and becomes stable with the increased curing time. Moreover, the overlay of BE-CIR pavement was paved after 7 days of curing, by which time most of the moisture had evaporated. Therefore, the XCT scanning test was performed after curing for 3 days and 7 days, and each specimen was finally scanned three times.

The XCT scanning test was conducted by a CT equipment model phoenix v|tome|x. A voltage of 140kV was applied with an electric current of 72μA, so it can emit more dense X-rays and obtain images based on high-frequency algorithms. The effective voxel size was set to 60.1μm. In this case, there was some difference in the number of cross-sections per sample due to the presence of the waterproofing layer, around 1830 two-dimensional cross-sections (slices of 1747 pixels x 1747 pixels) could be acquired from each specimen. In order to eliminate the edge effect, the middle 1750 slices were selected for further analyze.

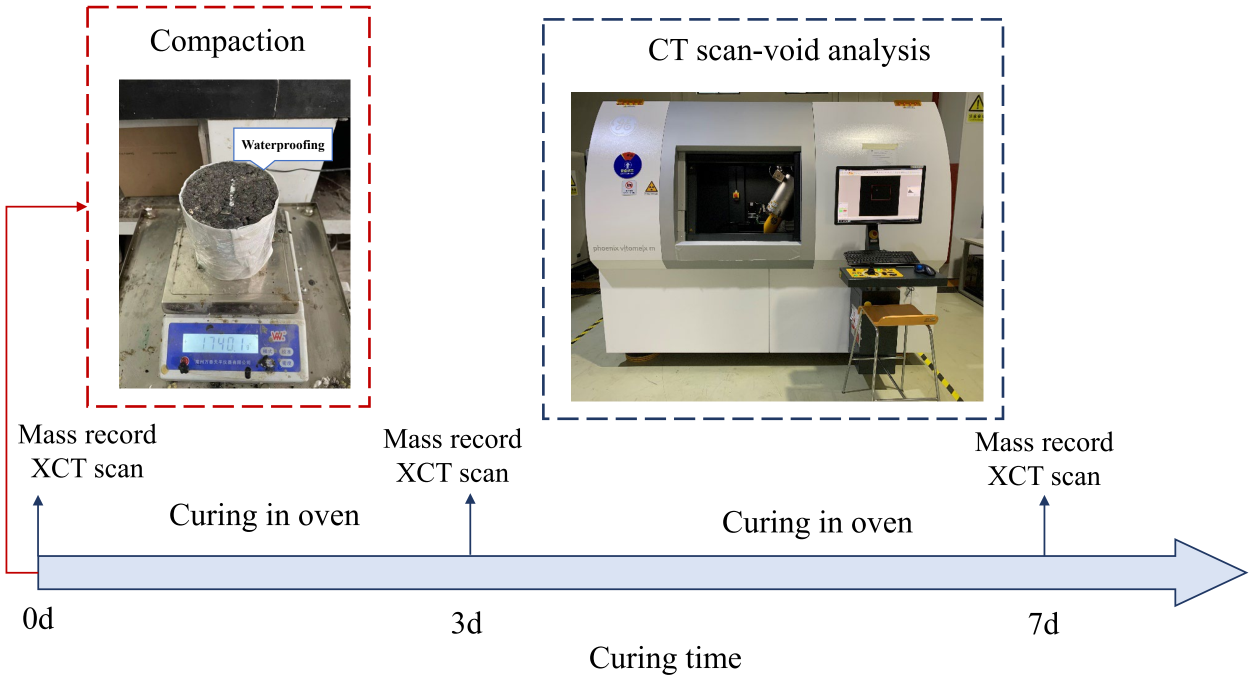


Figure 2 Overall experimental program

## 3 Image Analysis Method

### 3.1 Extraction of air void

Figure 3 illustrates a typical process of air void extraction from original XCT slice of BE-CIR. The original slice image is a grayscale image where the pixels of different grayscale represent different densities of materials. Due to the complex composition of the BE-CIR, the slice image actually contains four phases: coarse aggregate, asphalt mastic, moisture and air voids. The density of air voids are nearly zeros and represented by the pixels with the color of black in the slice. The brighter color in the slice represents the remaining three phases, of which coarse aggregate has the greatest density and is also clearly identifiable in the image. And although moisture has a smaller density than asphalt mastic, the gap is so small that it is difficult to separate it out individually. Therefore, only the air void could be extracted by processing the original XCT slice, and MATLAB was used in this paper for image processing. The image should be pre-processed before the segmentation to eliminate noise and uneven brightness in the image. The median filter algorithms and the top-hat transformation was applied in the image pre-processing [46]. To make the edges of the voids clearer, a contrast stretching function was also adopted to enhance the original slices.

The key point in the process of image segmentation is to determine the threshold gray level that could distinguish the air void and mixture entity. Since there may be different brightness of images at different height, specific thresholds should be confirmed for each XCT slice. So, a self-adaptive algorithm developed by Otsu was applied to find out the optimum thresholds of each XCT slice[47]. The principle of this method is minimizing the within-class variance while maximizing the mean variance of the two classes representing gray levels greater than and less than the threshold respectively[48]. Finally, the pixels representing air void could be extracted according to the threshold gray level, and then convert the slice image to binary image that consisted of only black (0 value) and white (1 value). As shown in Figure 3c, the binary image was ready for further analysis where the white pixels represent the air voids in the BE-CIR mixtures.

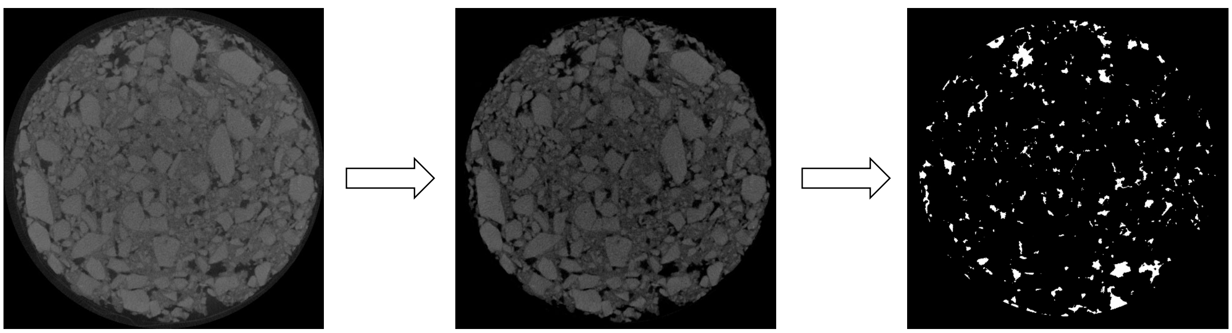

(a) original slice (b) pre-processed slice (c) binary image of air voids

Figure 3 A typical slice of air void extraction.

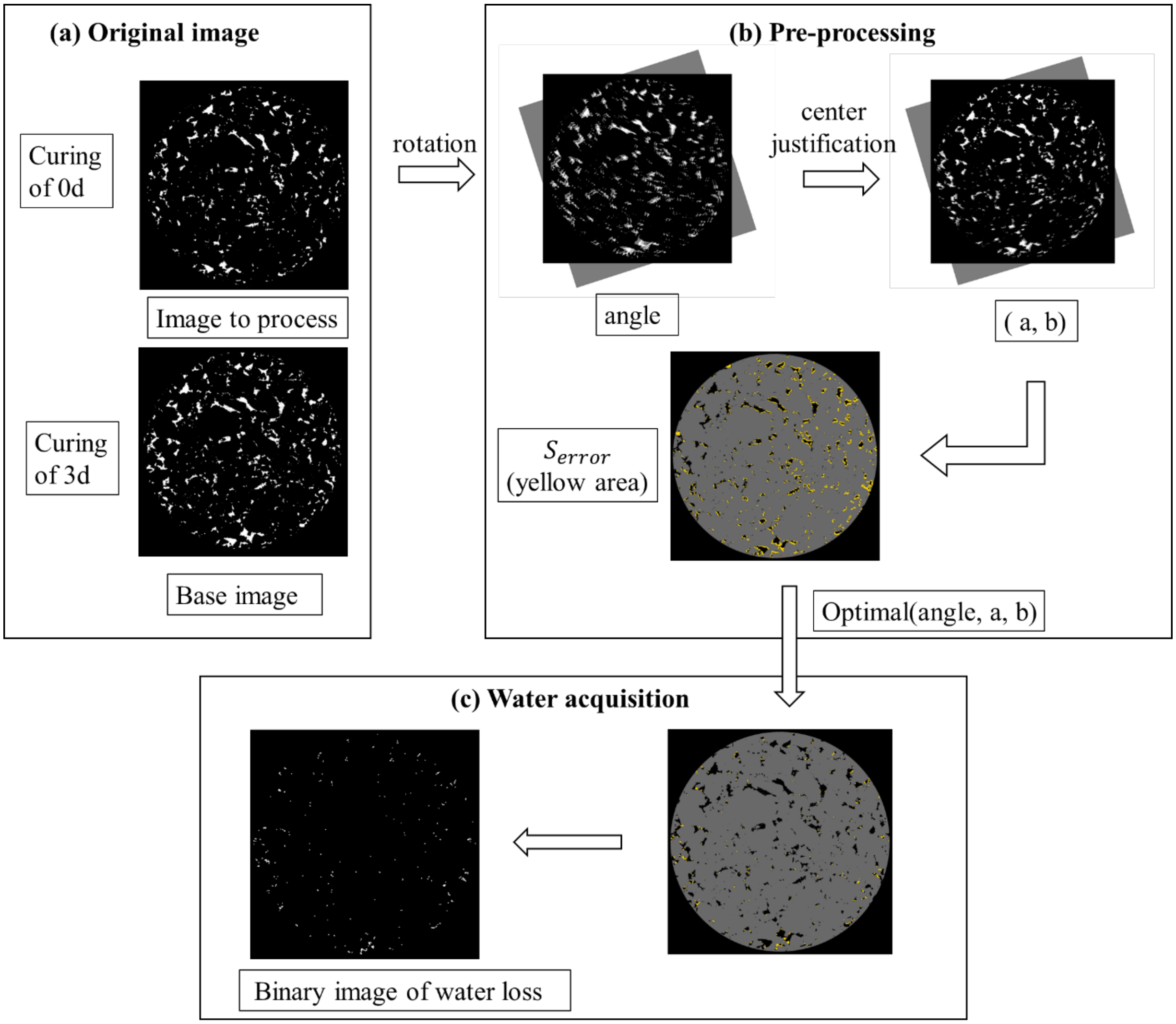


Figure 4 Acquisition process of water loss.

### 3.2 Identification of the moisture

During the curing process of BE-CIR mixture, the increase of air void may be influenced by many factors, including compact (which would happen under traffic in the field), water evaporation, porous networked structure formation, cement hydration, and some deformation due to evaporation kinetics and so on. On the one hand, since in this study the specimens were not subjected to compact during the curing, the change in air void due to rotational of the aggregates was not considered. On the other hand, the void changes caused by cement hydration and some deformation due to evaporation dynamics are relatively minor, often on the order of nanometres or a few microns. Meanwhile, these voids account for a relatively small proportion of the volume change and also hardly to be observed and extracted from the method of XCT scanning at mixture scale. Based on this, the variation of these small voids was ignored in this research. Therefore, it can be approximated that the increase in air void volume at different curing times is the decrease in moisture. This water dissipation is most often caused by continuous evaporation of water, but there is also a part that is consumed during rapid gelation (creating a highly porous networked structure within what was initially emulsion in the early stages of curing.

Based on the hypotheses above, the spatial structure of the moisture variation can be obtained by performing a difference calculation on the binary image of air voids (Figure 3c) under different curing days. However, as the location of the specimens cannot be the same on different curing days when conducting a CT scanning test, pre-processing is required to do different calculations on the binary image of air voids. Figure 4a shows the original images before processing. Because specimens curing for more days had higher air void content, the white pixels representing the air void in the corresponding image had a larger area and were therefore regarded as the base image for comparison. The pre-processing process consisted of rotation and center justification conducted on the image to process as illustrated in Figure 4b. The pre-processing starts with a pre-determined rotation angle based on the observation. Similarly, a pre-determined number (a, b) of floating pixels for the image to process was confirmed, where a was the number of pixels shifted horizontally in the image and b was the number of pixels shifted vertically in the image. To obtain the optimal rotation angle and (a, b), a Boolean operation was performed between the image to process and the base image using MATLAB. $S_{error}$ is defined as the intersection of the white pixels in the two images minus the concatenation of the white pixels, which is the non-overlapping area of the air void in the two images, as shown in the yellow area in Figure 4b. When $S_{error}$ was minimized, the corresponding (angle, a, b) was the optimal combination.

Finally, the image to process was transformed based on the optimal (angle, a, b), and the comparison was conducted with the base images. By comparing the white pixel of two image, the pixels that are white in the base image but not in the image to process were extracted as shown in Figure 4c. In fact, this binary image is the increase in air void and is also considered to be the dissipation of water.

### 3.3 Micro-morphology analysis of the water film

According to the binary image of water loss, several morphologic parameters are calculated to evaluate the process of water migration. By extracting the image features based on MATLAB, the area of each small white area in the image can be captured. The number of water particle $N_{wl}$ was defined as the number of the white area, and the water content of each slice $C_{wl}$ was defined as Eq.1. In addition, in order to evaluate the radial distribution of water particle, the average distance of all water particle with sample center in each slice $D_{wl}$ was defined as Eq.2 and Eq.3. Figure 5 illustrate some morphological parameters of water particle for better understanding.

$$C_{wl} = \frac{\sum Area_w^i}{A_{sample}} \quad (1)$$

$$D_{wl} = \frac{\sum Distance_w^i \cdot Area_w^i}{C_{wl} \cdot N_{wl}} \quad (2)$$

$$Distance_w^i = \sqrt[2]{(x_i - x_0)^2 + (y_i - y_0)^2} \quad (3)$$

Where $C_{wl}$ = the water content of each slice; $Area_w^i$ = area of each water particle; $A_{sample}$ = area of all sample range; $Distance_w^i$ = distance between the centroid of each water particle with the center of sample area; $D_{wl}$ = average distance of all water particle with sample center in each slice.

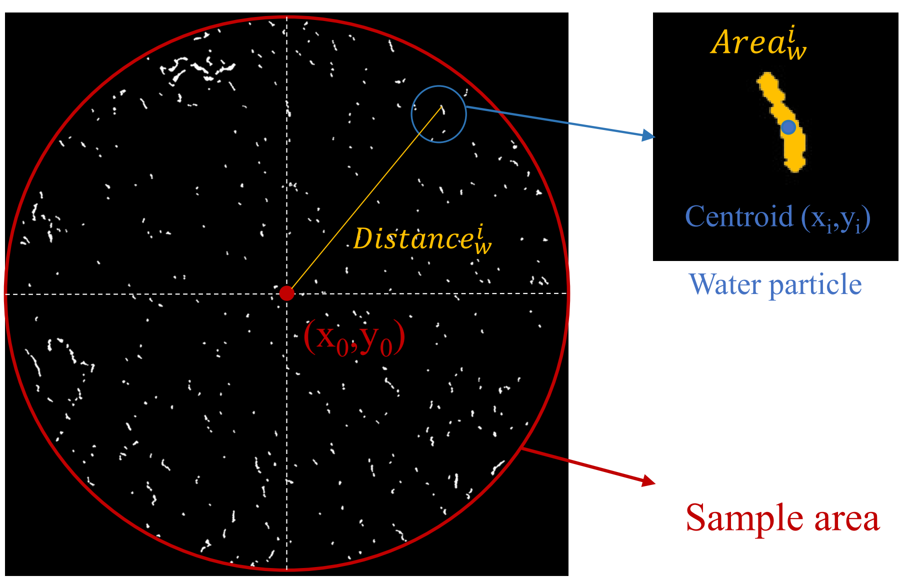


Figure 5 Morphological parameters of water particle

In addition to content and number, another important morphological parameter is the average size of the water particles. Normally, for example for air void analysis of asphalt mixtures, the average size is often evaluated by the equivalent diameter, that is, each void is approximated as a circle and its diameter is inverted by the area. However, due to the mobility of the water particles, the morphology of water particles may be elongated and not have a high degree of circularity as shown in Figure 6. The method of equivalent diameter is inaccurate in this situation. This paper uses a morphological calculation method by MATLAB to achieve water thickness. Figure 6 illustrates the procedures to calculate the water film thickness. First, the midcourt line of each area is extracted. Then the distance transformer was performed to obtained the thickness of each pixel of the midcourt line. The distance is recorded and the water thickness $T_{wl}$ of this point is defined as twice this distance.

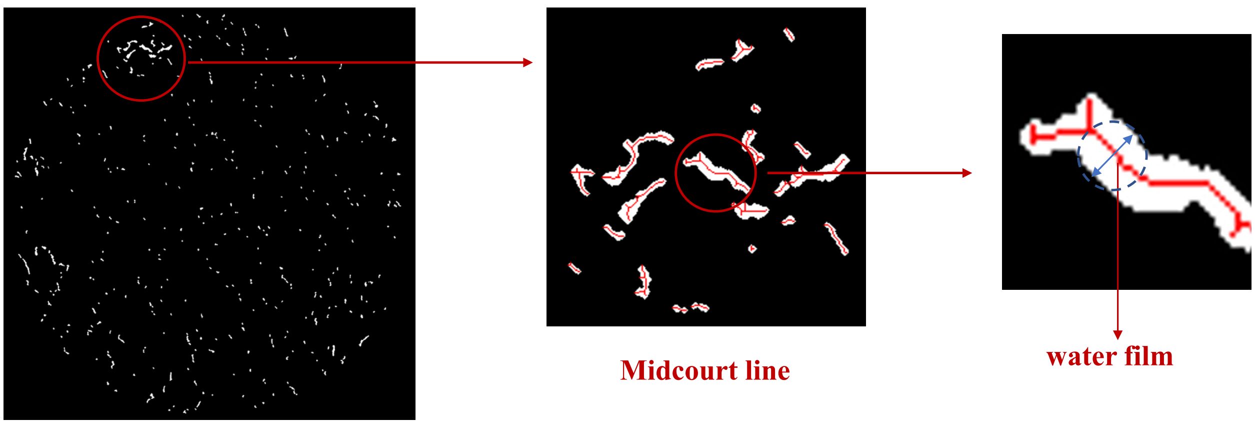


Figure 6 Procedures to calculate the water thickness

## 3.4 Mathematical model

To quantify the distribution of the water thickness $T_{wl}$, the spectrum of $T_{wl}$ was calculated by an interval of 0.1 mm. The percentage of accumulative water thickness within each interval on the total length of water thickness was calculated instead of the frequency of water thickness within the interval according to a previous study[49]. The distribution curve could be fitted by a logarithmic normal distribution model as showed in Eq.4:

$$f(T) = \frac{1}{10T\sigma\sqrt{2\pi}} \cdot e^{-\frac{(lnT-\mu)^2}{2\sigma^2}} \quad (x > 0) \qquad (4)$$

Where $T$ = water thickness; $f(T)$ = percentage of the segmented accumulative thickness on total thickness; $\sigma$, $\mu$ = the regression coefficients.

Figure 7 illustrates the actual value and fitting curve of $T_{wl}$ distribution. It could be found that the logarithmic normal distribution could fit well with the $T_{wl}$ distribution. Three different indices including peak value, mode, and expected value were proposed to characterize the logarithmic normal distribution model. As shown in Figure 7, the x-coordinate and y-coordinate of the peak point of distribution curve were defined as mode and peak value, which represent the dominated water thickness and its proportion respectively. The definition of the expected value which describes the average of the water thickness is exhibited in Eq.5.

$$E(T) = \int_{0}^{+\infty} T \cdot f(T)dT \qquad (5)$$

Where $T$ = water thickness; $f(T)$ = percentage of the segmented accumulative thickness on total thickness; $E(T)$ = the expected value of $f(T)$.

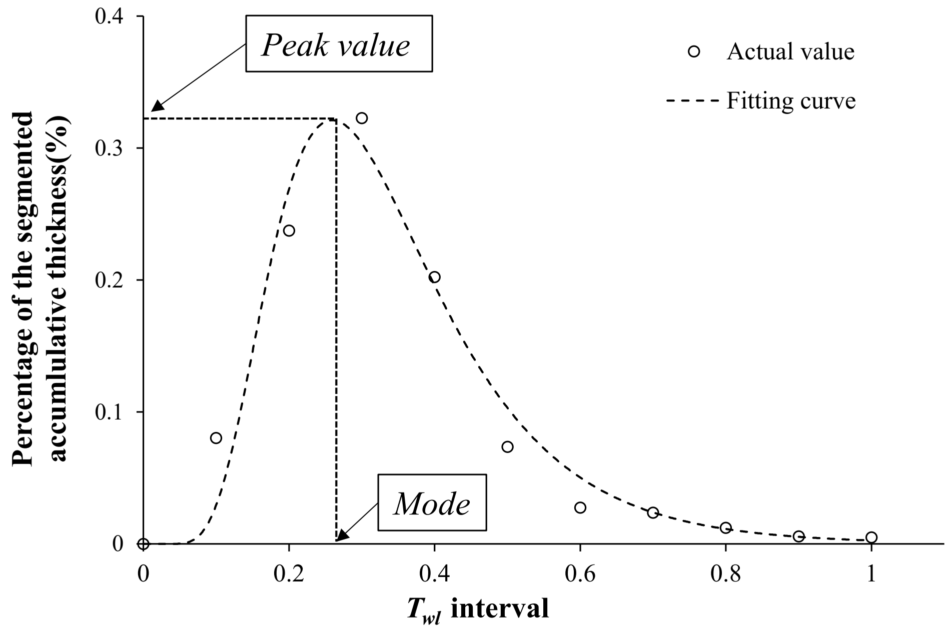


Figure 7 Mathematical model for water thickness distribution

# 4 Results and discussion

## 4.1 Weight loss

The weight loss is defined by Eq. (6), and Figure 8 illustrates the weight loss during curing time. The two time periods 0-3d and 3-7d have significantly different rates of change in weight loss. In curing time of 0-3d, the weight loss increased rapidly due to a greater moisture content and faster water evaporation. After curing for 3d, the weight loss gradually stabilized. Comparing two BE-CIR mixtures with different curing temperatures, BE-CIR1 showed a greater weight loss due to the higher curing temperature. The weight loss of BE-CIR1 was greater during 0-3 days of curing, while at 3-7 days the weight loss slowed down and the mass loss of BE-CIR2 varied considerably more. Thus, in view of the water losses during the curing, the influence of the curing temperature difference was greater at the first stage of curing (0-3d).

$$\text{Weight loss} = (m_i - m_0)/m_0 \quad (6)$$

Where $m_i$ represents the mass of specimen at curing time of $i$ days (g), $m_0$ is the mass of the specimen at 0h(g).

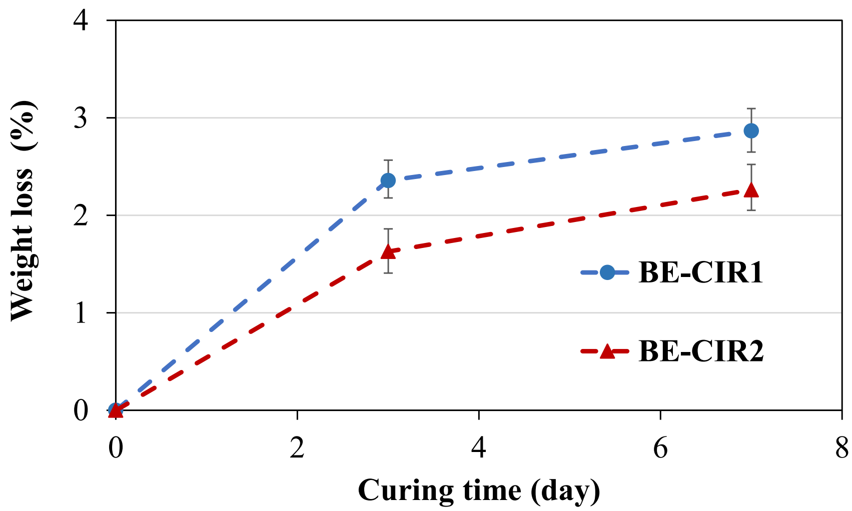


Figure 8 Variation of weight loss over curing time

### 4.2 Calculation of air void content

According to processing the binary images of air void, the air void content of each slice is defined by the area percent of air voids, and the overall air void content of a specimen approximately equals the average air void content in each cross-sectional CT slice. Figure 9 shows the variation of the overall and slice air void content with the curing time. Obviously, with the increase of curing time, the air void content of each BE-CIR increased continuously because of the evaporation of water inside the mixture. From Figure 9a, the original air void content of BE-CIR1 (4.93%) and BE-CIR3 (5.02%) was similar, and the error between parallel specimens was small. Considering the increment of air void content during curing, since BE-CIR1 has higher curing temperature than BE-CIR2, it had a greater mass loss, resulting in higher air void content. Meanwhile, similar to mass loss, the growth of air void content of BE-CIR1 between 0-3d was larger than that of BE-

CIR3, while it was smaller between 3-7d. In addition, the error between the parallel specimens showed a certain degree of increase over curing time, and the variability of air void content was relatively larger at lower curing temperature. Despite of this, the variation of the samples after curing for 7 days was within 5%.

The distributions for air void content at different depths of BE-CIR specimens were plotted in Figure 9 (b, c). The depth of 0mm was the surface that was not covered by the waterproof. As the specimen had a height of 10cm, the depth of the bottom surface was 100mm. It is obvious that the curves in Figure 9(b, c) show a ‘‘bathtub’’ shape, which indicates that the SGC compaction produces more air voids at the top and bottom parts of a specimen. With the increasing curing time, the air void content became larger at all locations in the depth direction. However, the magnitude of variation at different depths and the variability pattern between curing time intervals differed. This is due to the bottom-up migration of water as well as evaporation, and this water gradient migration characterization will be discussed in the next sections.

It is worth noting that the curing method used in determining the number of gyrations is an accelerated curing method, i.e. specimens was unsealed and cured in oven at 60℃ for 48 hours [34]. In that situation, the water inside the mixture could evaporate almost completely, while the semi-sealed laboratory curing condition used in this paper may result in incomplete evaporation of water, so that the air void of three BE-CIR at 153h was smaller than the target air void of 10%.

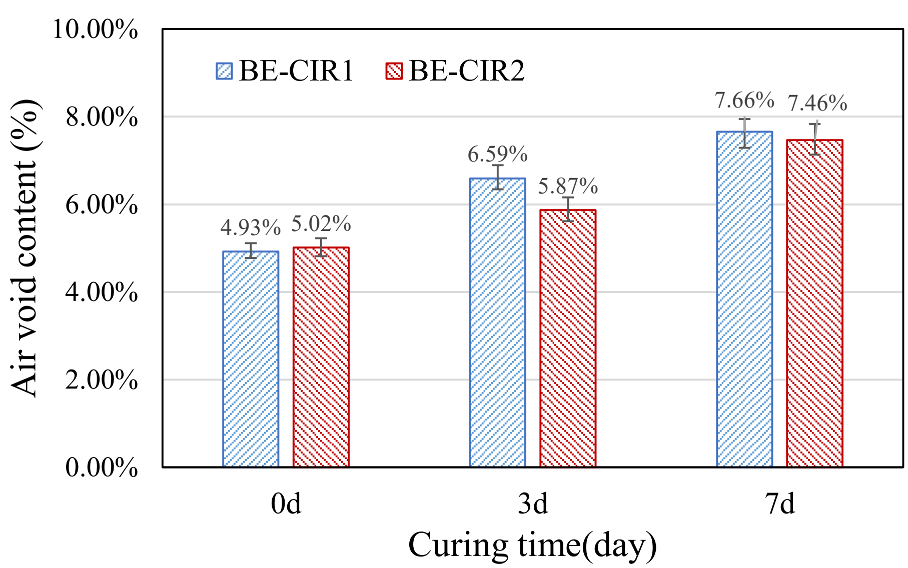


(a)

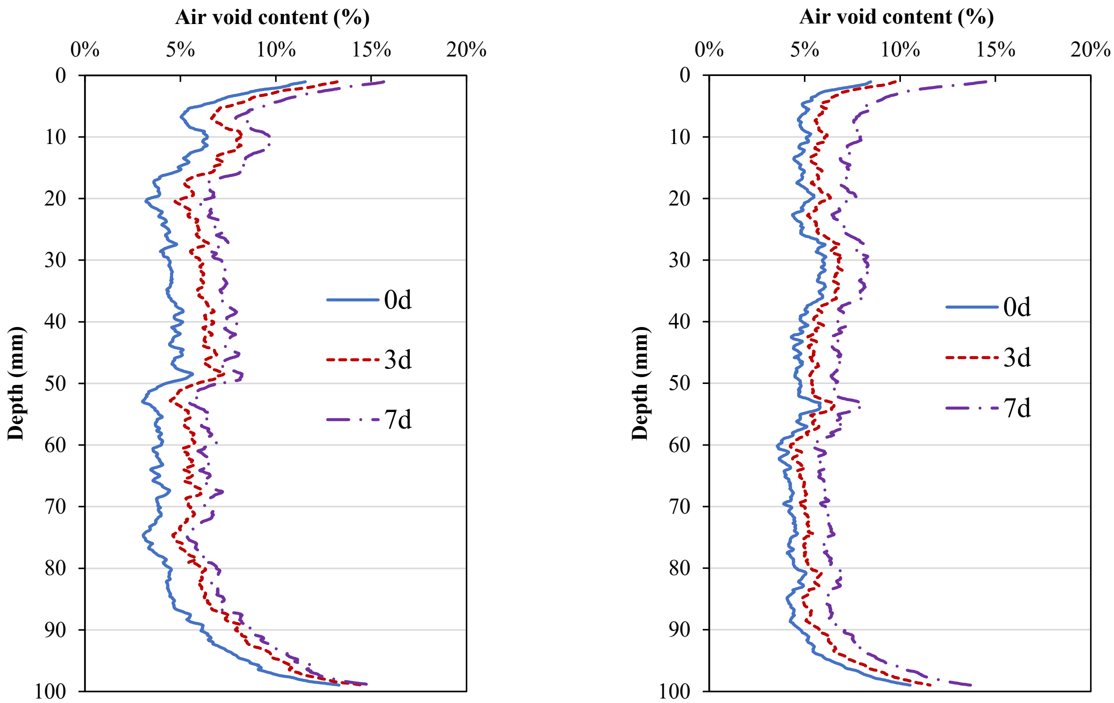


(c) (d)

Figure 9 Variation of overall air void content: (a) variation of air void content over curing time, (b) air void content of BE-CIR1 in the depth direction, (c) air void content of BE-CIR2 in the depth direction.

## 4.3 Water variation of whole curing process (0-7d)

### *4.3.1 Results of $C_{wl}$ and $N_{wl}$*

Figure 10 illustrates the results of $C_{wl}$ and $N_{wl}$ in depth direction after curing for 7 days. It can be seen from Figure 10a that the $C_{wl}$ are larger at lower depth, which means the water loss near the surface is significantly higher. Comparing the two BE-CIRs, the $C_{wl}$ was greater for BE-CIR1 which had a higher curing temperature. In the depth direction, $C_{wl}$ of BE-CIR1 showed a pronounced decrease from 0-90mm. While $C_{wl}$ of BE-CIR2 only displayed a significant decrease from 0-40mm, the content of water loss was essentially the same between 40-90 mm. In addition, $C_{wl}$ increased with depth at 90-100mm, probably due to the fact that that water near the bottom will flow downwards by the effect of gravity.

Number of water loss in the depth direction was shown in Figure 10b. Similar to the results of $C_{wl}$, the $N_{wl}$ of BE-CIR1 decreased consistently with the depth increased. In contrast, BE-CIR2 only decreases significantly from 0-40 mm and $N_{wl}$ increased markedly at depths of 90-100 mm.

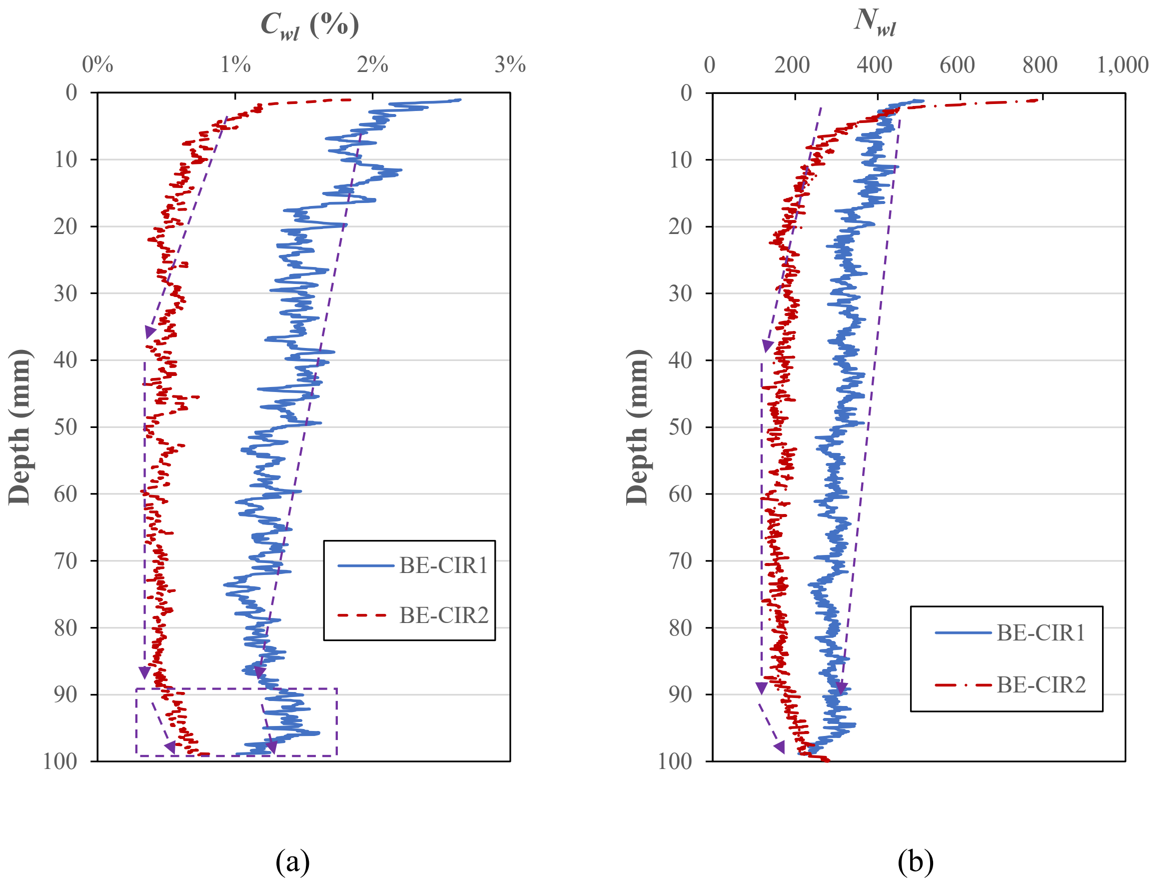


Figure 10 Results of $C_{wl}$ and $N_{wl}$ after curing 7 days: (a) variation of $C_{wl}$ in the depth direction, and (b) variation of $N_{wl}$ in the depth direction,

*4.3.2 Results of water film thickness*

Figure 11 shows the water thickness $T_{wl}$ of two BE-CIRs in the depth direction and the logarithmic normal distribution model. The logarithmic normal distribution model was fitted by the average of $T_{wl}$ at all depth in each interval. The regression parameters and three indices of $T_{wl}$ are also presented in the figure. It is found that the $R^2$ are much closer to 1, which means that the two-parameter logarithmic normal distribution model can fit the water film thickness distribution well. The average $T_{wl}$ was essentially the same at different depths of each specimen and did not exhibit the gradient characteristics as $C_{wl}$ and $N_{wl}$. From the indices calculated by logarithmic normal distribution model, BE-CIR1 demonstrate a smaller peak value, larger mode and larger expected value than BE-CIR2, which also demonstrate that higher curing temperature could cause more water to evaporate from the pores.

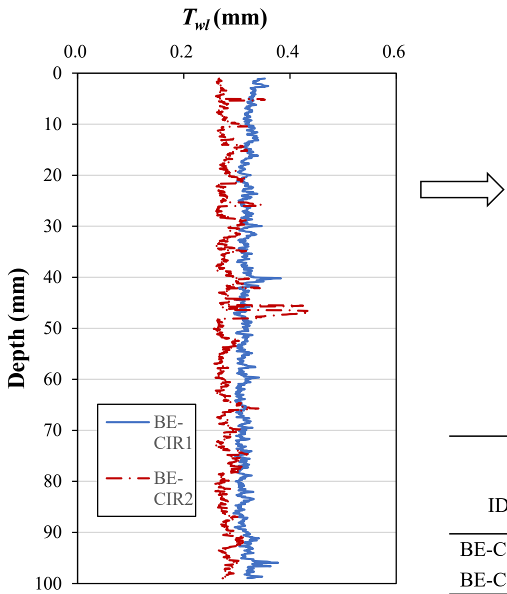

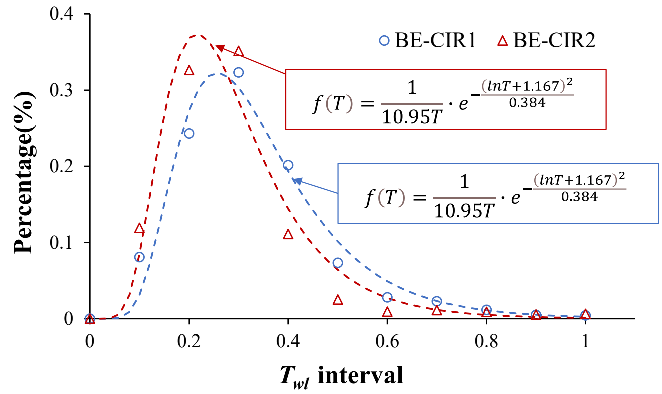


| ID | Logarithmic normal distribution model | | | Indices for water thickness | | |
|---|---|---|---|---|---|---|
| | $\sigma$ | $\mu$ | $R^2$ | Expected value(mm) | Mode(mm) | Peak value (%) |
| BE-CIR1 | 0.437 | 1.167 | 0.952 | 0.338 | 0.257 | 32.28 |
| BE-CIR2 | 0.447 | 1.333 | 0.937 | 0.290 | 0.216 | 37.42 |

Figure 11 Results of water thickness in the depth direction and mathematical model

## 4.4 Water variation of different curing stages

*4.4.1 3D-reconstruction and radial distribution*

In order to analyze the variation of moisture under the two different curing stages of 0-3 days and 3-7days, the 3D reconstruction of the moisture variation was conducted on different curing periods as illustrated in Figure 12(a). Meanwhile, the results of $D_{wl}$ in the depth direction were also presented along with the 3D model. The larger $D_{wl}$ means that the moisture distribution is more towards the edge of the sample at this cross section. There was obviously more water distribution in BE-CIR1 than BE-CIR2 during the curing period 0-7d. It could be found that more moisture accumulation at the edge of BE-CIR2 which lead to the $D_{wl}$ of BE-CIR2 was greater than that of BE-CIR1. Considering the $D_{wl}$ in the depth direction, BE-CIR1 with the higher curing temperature had a more uniform distribution, while the BE-CIR2 had a larger $D_{wl}$ the closer to the surface. Comparing two different curing stages, the moisture variation of BE-CIR1 in 0-3d presents apparently greater volume than that in 3-7d, while BE-CIR2 was quite different. Some larger volume of moisture appeared at the edge of BE-CIR2 during the curing period of 0-3d, resulting in the largest $D_{wl}$ of all samples. The number of water particles in 3-7d of BE-CIR2 was more intensive than 0-3d, and more often distributed inside the specimen.

Furthermore, the average $D_{wl}$ of all slices was calculated as shown in Figure 12(b). Theoretically, if the water particles are uniformly distributed on each slice, since the sample radius was 50 mm, the value of $D_{wl}$ should be close to half of the radius, i.e. 25 mm. However, it can be found from Figure 12 (b) that the $D_{wl}$ under all curing stages is greater than 25mm, which may be due to the fact that the prepared specimens were not completely uniform in the radial direction and there were some large voids near the edges, making more channels for moisture migration. The average $D_{wl}$ for both BE-CIR during 0-3d was about 5 mm larger than that of 3-7d and was closer to 25mm. This indicates that there was also an inner-to-outer evaporation path in the radial distribution of the moisture migration behavior.

*4.4.2 Results of $C_{wl}$ and $N_{wl}$*

Figure 13 presents the trend of $C_{wl}$ in the depth direction for both BE-CIRs. It can be observed that $C_{wl}$ remained essentially constant in the depth direction during the first three curing days, while there was a significant gradient characteristic at 3-7 days which was similar with the variation of whole curing. Comparing the BE-CIR curing under two different temperatures, $C_{wl}$ of BE-CIR1 was greater under curing from 0-3days than from 3-7days, while BE-CIR2 exhibited the opposite pattern. Additionally, the depth range of the gradient characteristic differed between the two specimens during curing of 3-7 days, with the $C_{wl}$ of BE-CIR1 decreasing with depth increasing from 0mm to 80mm, while such a gradient characteristic existed only in the depth of 0-40mm for BE-CIR2. It can be demonstrated that higher curing temperature would result in more water loss in the first stage of curing, while for the second curing stage, temperature also affects the depth of water diffusion and evaporation. Moreover, the difference of $C_{wl}$ in the gradient distribution was also influenced by the curing temperature. For BE-CIR1, the difference of $C_{wl}$ could reach to approximately 0.8%, while the BE-CIR2 only presented a difference of 0.5%.

Figure 14 illustrates the results of $N_{wl}$ in the depth direction. It can be found that the trend of $N_{wl}$ in the depth direction was basically the same as $C_{wl}$. However, the difference with $C_{wl}$ was that for BE-CIR1, $C_{wl}$ of 0 to 3 days was greater than that of 3 to 7 days, while $N_{wl}$ of 0 to 3 days was, on the contrary, smaller than 3 to 7 days. Similarly, the trend can also be found from BE-CIR2, where the deference of number of $N_{wl}$ from 0-3 days and 3-7 days was significantly bigger than that of $C_{wl}$. It can be inferred that in the second stage of curing (3-7 days), the water dissipation is mainly in the form of capillary water, resulting in many small internal voids.

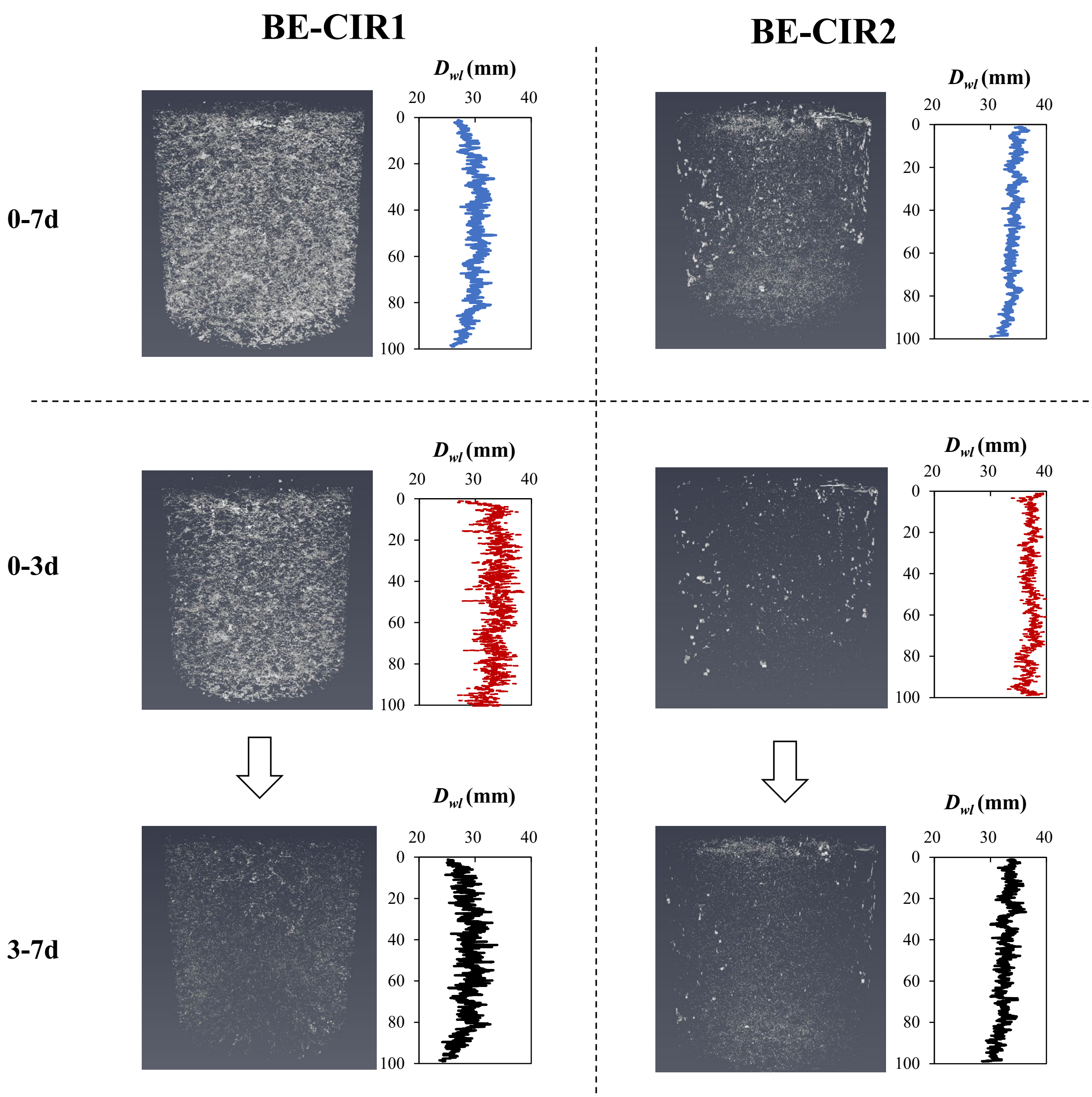


(a)

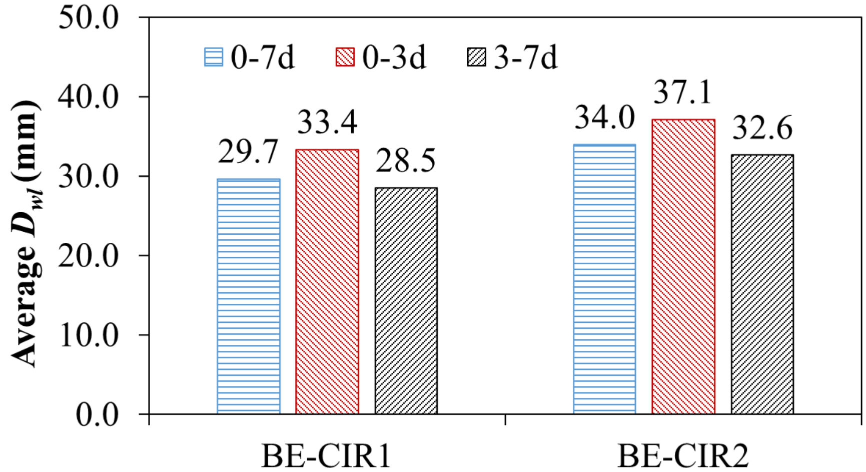


(b)

Figure 12 3D-reconstruction and radial distribution: (a) $D_{wl}$ in the depth direction (b) average $D_{wl}$ of different curing time.

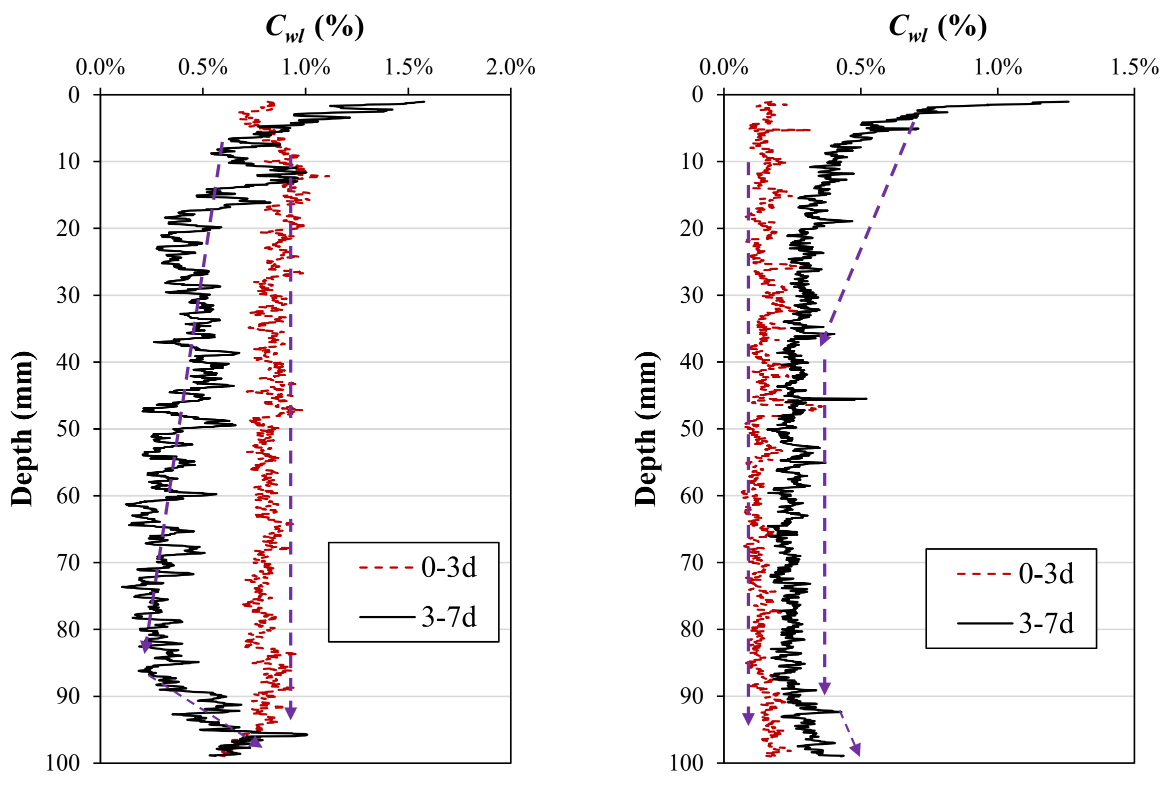


(a) BE-CIR1 (b) BE-CIR2

Figure 13 Results of $C_{wl}$ in different curing stage

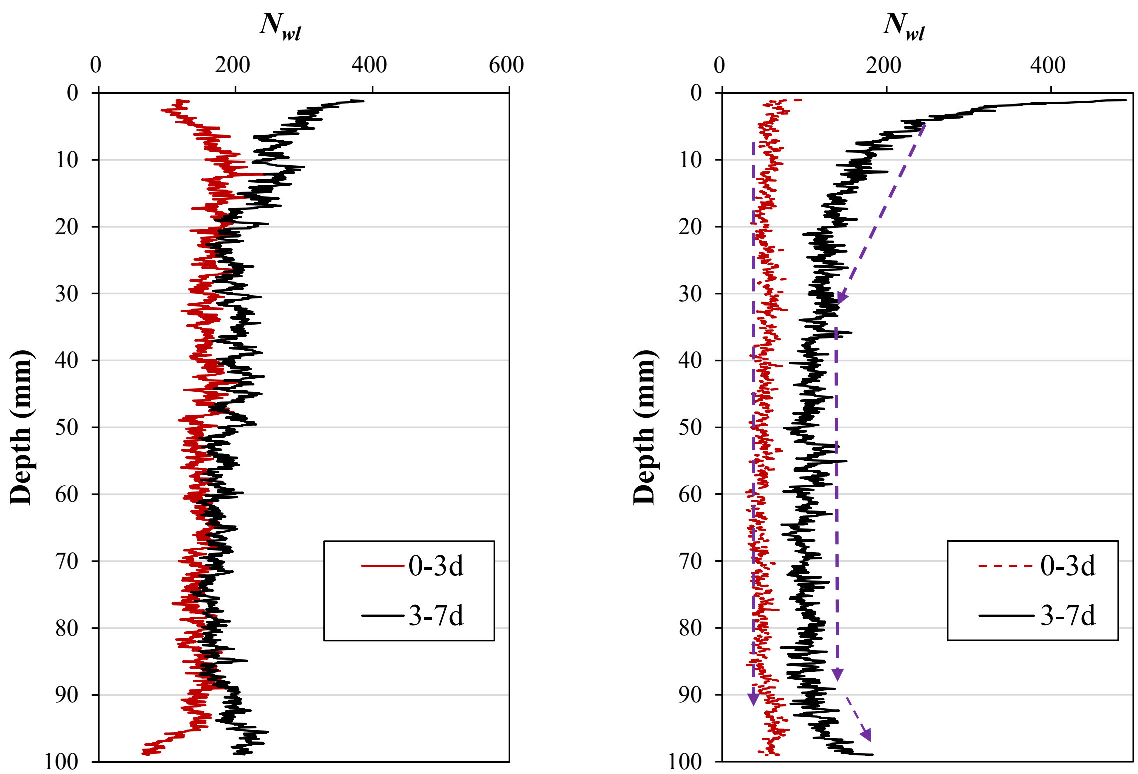


(a) BE-CIR1 (b) BE-CIR2

Figure 14 Results of $N_{wl}$ in different curing stage

### *4.4.3 Results of water film thickness*

The water thickness $T_{wl}$ of two different curing stage of each BE-CIR in the depth direction and the corresponding logarithmic normal distribution model is shown as Figure 15. From the perspective of variation in the depth direction, the average $T_{wl}$ at every curing stage was essentially the same in the depth direction. However, it is evident that the average $T_{wl}$ at 0 to 3 days fluctuated more at certain depth positions compared to 3-7d, especially more pronounced for BECIR2. This may be due to the fact that in the early stage of curing, the dominant dissipation of water is free water which could be a relative aggregation in the void at the initial state of specimen.

Similar with the whole curing, the mathematical model can also fit the water thickness distribution of each stage well, and the $R^2$ are greater than 0.9. As Figure 15 (a) shows, water thickness during curing time of 3 to 7 days presents higher peak value, lower mode and expected value than 0 to 3 days, which suggests that in the second stage, water dissipation is more likely to be in the form of capillary water. As for BE-CIR2 in Figure 15 (b), the mode of two curing stage was the same caused by a lower curing temperature, while peak value in the 3 to 7days was obviously higher than that of 0 to 3 days. It also indicates that in the second stage there is less water diffusion in the form of irregular and large particles, capillary water with a smaller thickness gradually dominating the dissipation.

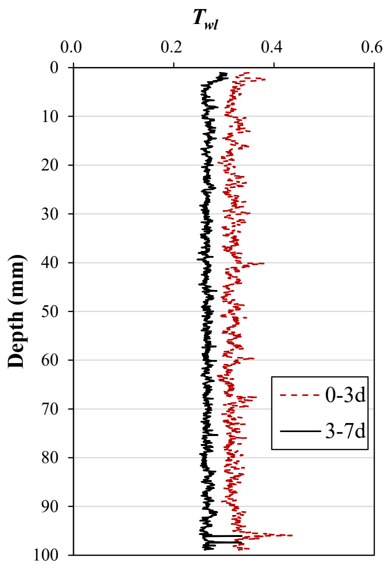


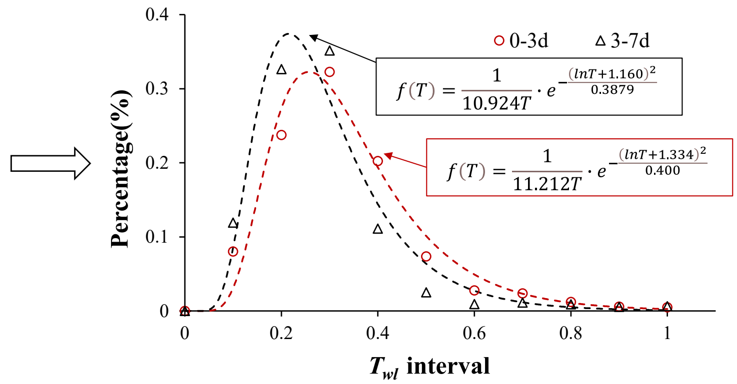


| ID | Logarithmic normal distribution model | | | Indices for water thickness | | |
|---|---|---|---|---|---|---|
| | $\sigma$ | $\mu$ | $R^2$ | Expected value(mm) | Mode(mm) | Peak value (%) |
| BE-CIR1 | 0.436 | 1.160 | 0.954 | 0.340 | 0.259 | 32.11 |
| BE-CIR2 | 0.447 | 1.334 | 0.937 | 0.289 | 0.216 | 37.41 |

(a) BE-CIR1

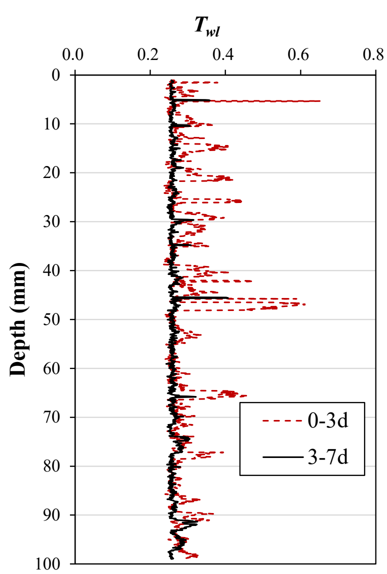


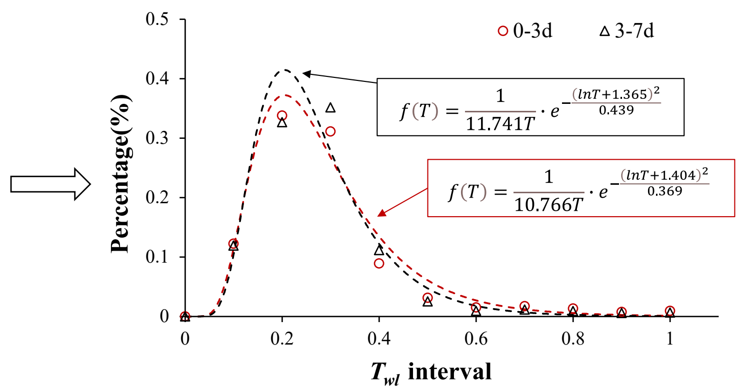


| ID | Logarithmic normal distribution model | | | Indices for water thickness | | |
|---|---|---|---|---|---|---|
| | $\sigma$ | $\mu$ | $R^2$ | Expected value(mm) | Mode(mm) | Peak value (%) |
| BE-CIR1 | 0.468 | 1.365 | 0.959 | 0.283 | 0.205 | 37.21 |
| BE-CIR2 | 0.429 | 1.404 | 0.933 | 0.269 | 0.204 | 41.47 |

(b) BE-CIR2

Figure 15 Results of water thickness in the depth direction and its distribution and mathematical model

## 5 Conclusions and Findings

In this paper, XCT scanning tests were used to investigate the moisture migration of BE-CIR mixtures during the curing process. The main conclusions and findings are as follows:

(1) The developed image processing method can identify the moisture distribution of BE-CIR mixtures by conducting a Boolean operation on pre-processed air voids binary images at different curing periods. The water migration behavior could be detailed described by the distribution and thickness of water droplets instead of only mass loss. The distribution of water thickness could fit well with the logarithmic normal distribution model.

(2) The variation of radial distribution with curing time indicates that there is an inside-out characteristic of moisture migration behavior in the radial direction. Decreasing the curing temperature can contribute to the accumulation of moisture at the edges, thus allowing more water to evaporate from the edges rather than the inside.

(3) The content of moisture distribution presents a gradient feature in the depth direction which is greater near the surface and smaller at the bottom. This is mainly due to the migration of water from the inside to the outside, and thus lead to the existence of about 0.5% of the residual moisture content difference inside the mixture at 7 curing days. The curing temperature could strongly affect the gradient migration behavior of water, as evidenced by the depth of the gradient feature, which is 0-90mm for BE-CIR1(40°C) and 0-40mm for BE-CIR2(25°C) respectively.

(4) The gradient characteristics of moisture distribution manifested only in the stage of 3 to 7d. Combined with results of water film thickness, it could be concluded that in the early stage of curing, most of the moving water exhibits thicker and more irregular $T_{wl}$, while moisture with a thinner thickness gradually dominates the migration with time. Higher curing temperature result in greater water film thickness, also indicating a faster rate of water migration.

The nanoscale moisture migration caused by the capillary water or hydration reaction was not included in this research due to the limitation of image precision and the back-calculation assumptions of air void change. Therefore, in the future, it is necessary to further go to the nano pores and nanoscale moisture migration with the help of more advanced testing methods, which can shed more lights on the microstructural formation of the BE-CIR mixtures.

**Acknowledgement**

This work was supported by the National Natural Science Foundation of China (Grant No. 52108421), the Hong Kong Research Grant Council through the GRF project (Grant No. 15220621), and the Fundamental Research Funds for the Central Universities (Grant No. 3221002139D).

## References


[1] J. Wang, Q. Li, Y. Lu, S.J.C. Luo, B. Materials, Effect of waste-oil regenerant on diffusion and fusion behaviors of asphalt recycling using molecular dynamics simulation, 343 (2022) 128043.

[2] F. Gu, W.Y. Ma, R.C. West, A.J. Taylor, Y.Q. Zhang, Structural performance and sustainability assessment of cold central-plant and in-place recycled asphalt pavements: A case study, Journal of Cleaner Production 208 (2019) 1513-1523.

[3] A. Modarres, M. Rahimzadeh, M. Zarrabi, Field investigation of pavement rehabilitation utilizing cold in-place recycling, Resources Conservation and Recycling 83 (2014) 112-120.

[4] J. Turk, A.M. Pranjic, A. Mladenovic, Z. Cotic, P. Jurjavcic, Environmental comparison of two alternative road pavement rehabilitation techniques: cold-in-place-recycling versus traditional reconstruction, JOURNAL OF CLEANER PRODUCTION 121 (2016) 45-55.

[5] A.E. Alkins, B. Lane, T. Kazmierowski, Sustainable Pavements Environmental, Economic, and Social Benefits of In Situ Pavement Recycling, TRANSPORTATION RESEARCH RECORD (2084) (2008) 100-103.

[6] F. Xiao, S. Yao, J. Wang, X. Li, S. Amirkhanian, A literature review on cold recycling technology of asphalt pavement, Construction and Building Materials 180 (2018) 579-604.

[7] S. Casillas, A.F.J.T.R.R. Braham, Development of a Performance-Based Approach to Asphalt Emulsion Selection for Cold In-Place Recycling Applications, 2676(5) (2022) 104-115.

[8] L.N. Mohammad, M.Y. Abu-Farsakh, Z. Wu, C. Abadie, Trb, Trb, Louisiana experience with foamed recycled asphalt pavement base materials, Bituminous Paving Mixtures 2003: Materials and Construction2003, pp. 17-24.

[9] K. Kuna, G. Airey, N. Thom, Mix design considerations of foamed bitumen mixtures with reclaimed asphalt pavement material, International Journal of Pavement Engineering 18(10) (2017) 902-915.

[10] Q. Lecuru, Y. Ethier, A. Carter, M.J.A.i.C.E.M. Karray, Characterization of cold in-place recycled materials at young age using shear wave velocity, 8(1) (2019) 336-354.

[11] A. Grilli, A. Graziani, E. Bocci, M. Bocci, Volumetric properties and influence of water content on the compactability of cold recycled mixtures, Materials and Structures 49(10) (2016) 4349-4362.

[12] S.W. Du, The Optimum Pre-mixing Water Content in Asphalt Emulsion Mixture with Cement, Journal of Testing and Evaluation 49(6) (2021) 4560-4575.

[13] D. Lesueur, J.J.J.R.M. Potti, P. Design, Cold mix design: a rational approach based on the current understanding of the breaking of bituminous emulsions, 5(sup1) (2004) 65-87.

[14] S. Raschia, C. Mignini, A. Graziani, A. Carter, D. Perraton, M.J.R.M. Vaillancourt, P. Design, Effect of gradation on volumetric and mechanical properties of cold recycled mixtures (CRM), 20(sup2) (2019) S740-S754.

[15] M. Miljković, L. Poulikakos, F. Piemontese, M. Shakoorioskooie, P.J.C. Lura, B. Materials, Mechanical behaviour of bitumen emulsion-cement composites across the structural transition of the co-binder system, 215 (2019) 217-232.

[16] L. Yongliang, K. Xiangming, Z. Yanrong, Y.J.J.o.M.i.C.E. Peiyu, Static and dynamic mechanical properties of cement-asphalt composites, 25(10) (2013) 1489-1497.

[17] M. Miljković, L. Poulikakos, F. Piemontese, M. Shakoorioskooie, P. Lura, Mechanical behaviour of bitumen emulsion-cement composites across the structural transition of the co-binder system, Construction and Building Materials 215 (2019) 217-232.

[18] J. Ouyang, J. Zhao, Y.J.J.o.M.i.C.E. Tan, Modeling mechanical properties of cement asphalt emulsion mortar with different asphalt to cement ratios and temperatures, 30(10) (2018) 04018263.

[19] L. Ziyani, V. Gaudefroy, V. Ferber, F.J.C. Hammoum, S.A. Physicochemical, E. Aspects, A predictive and experimental method to assess bitumen emulsion wetting on mineral substrates, 489 (2016) 322-335.

[20] Ö. Çakır, F.J.C. Aköz, B. Materials, Effect of curing conditions on the mortars with and without GGBFS, 22(3) (2008) 308-314.
[21] A. García, P. Lura, M.N. Partl, I.J.M. Jerjen, structures, Influence of cement content and environmental humidity on asphalt emulsion and cement composites performance, 46 (2013) 1275-1289.
[22] S. Martínez-Ramírez, M.J.C. Frías, B. Materials, The effect of curing temperature on white cement hydration, 23(3) (2009) 1344-1348.
[23] A. Graziani, C. Godenzoni, F. Cardone, M. Bocci, Effect of curing on the physical and mechanical properties of cold-recycled bituminous mixtures, Materials & Design 95 (2016) 358-369.
[24] P. Orosa, I. Pérez, A.R. Pasandín, Short-term resilient behaviour and its evolution with curing in cold in-place recycled asphalt mixtures, Construction and Building Materials 323 (2022) 126559.
[25] W.T. Yang, J. Ouyang, Y. Meng, B.G. Han, Y.Q. Sha, Effect of curing and compaction on volumetric and mechanical properties of cold-recycled mixture with asphalt emulsion under different cement contents, Construction and Building Materials 297 (2021).
[26] B.C. Cox, I.L. Howard, C.S. Campbell, Cold In-Place Recycling Moisture-Related Design and Construction Considerations for Single or Multiple Component Binder Systems, Transportation Research Record (2575) (2016) 27-38.
[27] B.C. Cox, I.L. Howard, Cold in-place recycling characterization framework and design guidance for single or multiple component binder systems, 2015.
[28] A. Woods, Y. Kim, H. Lee, Determining Timing of Overlay on Cold In-Place Recycling Layer Development of New Tool Based on Moisture Loss Index and In Situ Stiffness, Transportation Research Record (2306) (2012) 52-61.
[29] A. Banerjee, A.D. Smit, J.A. Prozzi, Modeling the effect of environmental factors on evaporative water loss in asphalt emulsions for chip seal applications, Construction and Building Materials 27(1) (2012) 158-164.
[30] M. Miljković, M.J.M. Radenberg, Structures, Characterising the influence of bitumen emulsion on asphalt mixture performance, 48 (2015) 2195-2210.
[31] S. Raschia, T. Chauhan, S. Panwar, A. Carter, A. Graziani, D. Perraton, Effect of water and cement content on the mechanical properties of cold recycled mixtures (CRM) with bitumen emulsion, Proceedings of the 5th International Symposium on Asphalt Pavements & Environment (APE) 5, Springer, 2020, pp. 274-282.
[32] T. Saadoon, B. Gomez-Meijide, A. Garcia, Prediction of water evaporation and stability of cold asphalt mixtures containing different types of cement, Construction and Building Materials 186 (2018) 751-761.
[33] T. Saadoon, A. Garcia, B.J.M. Gómez-Meijide, Design, Dynamics of water evaporation in cold asphalt mixtures, 134 (2017) 196-206.
[34] J. Ouyang, Y. Meng, T. Tang, M. Miljković, Y.J.C. Tan, B. Materials, Characterization of the drying behaviour of asphalt emulsion, 274 (2021) 122090.
[35] D. Lesueur, C. Coupé, M.J.R.M. Ezzarougui, P. Design, Skin formation during the drying of a bitumen emulsion, 2(2) (2001) 161-179.
[36] M. Goavec, S. Rodts, V. Gaudefroy, P. Faure, P.J.C. Coussot, S.A. Physicochemical, E. Aspects, Magnetic resonance imaging of drying bitumen emulsions, 591 (2020) 124512.
[37] L. Meknaci, A. Graziani, C. Mignini, A.D. Henni, M.J.R.M. Miljković, P. Design, Influence of bitumen emulsion on the curing behaviour of standardised cold bitumen emulsion mortars, 23(sup1) (2022) 99-115.
[38] M. Miljković, M.J.M. Radenberg, Structures, Effect of compaction energy on physical and mechanical performance of bitumen emulsion mortar, 49 (2016) 193-205.
[39] M. Miljković, M. Radenberg, X. Fang, P.J.M. Lura, Structures, Influence of emulsifier content on cement hydration and mechanical performance of bitumen emulsion mortar, 50 (2017) 1-14.

[40] T. Saadoon, A. Garcia, B. Gómez-Meijide, Dynamics of water evaporation in cold asphalt mixtures, Materials & Design 134 (2017) 196-206.
[41] A. Grilli, S. Raschia, D. Perraton, A. Carter, A. Rahmanbeiki, P. Kara De Maeijer, D. Lo Presti, G. Airey, C. Ogbo, E.V. Dave, Experimental investigation on water loss and stiffness of CBTM using different RA sources, Proceedings of the RILEM International Symposium on Bituminous Materials: ISBM Lyon 2020 1, Springer, 2022, pp. 11-17.
[42] R. Li, Z. Leng, Y. Wang, F. Zou, Characterization and correlation analysis of mechanical properties and electrical resistance of asphalt emulsion cold-mix asphalt, Construction and Building Materials 263 (2020) 119974.
[43] Z.L. Zhao, J.W. Jiang, Z.W. Chen, F.J. Ni, Moisture migration of bitumen emulsion-based cold in-place recycling pavement after compaction: Real-time field measurement and laboratory investigation, Journal of Cleaner Production 360 (2022).
[44] J.P. DOT, Applied Manual for Asphalt Emulsion Cold In-Place Recycling Technology, China, 2010.
[45] MOT, Technical Specifications for Highway Asphalt Pavement Recycling (in Chinese). Ministry of Transport of the People’s Republic of China., 2019.
[46] K. Gopalakrishnan, N. Shashidhar, X. Zhong, Attempt at quantifying the degree of compaction in HMA using image analysis, Advances In Pavement Engineering2005, pp. 1-15.
[47] L. Gao, F. Ni, H. Luo, S. Charmot, Characterization of air voids in cold in-place recycling mixtures using X-ray computed tomography, Construction and Building Materials 84 (2015) 429-436.
[48] N.J.I.t.o.s. Otsu, man,, cybernetics, A threshold selection method from gray-level histograms, 9(1) (1979) 62-66.
[49] J. Jiang, F. Ni, L. Yao, X. Cui, Evaluating the mastic distribution of asphalt mixtures based on a new thickness threshold using 2D image planers, Road Materials and Pavement Design 19(6) (2017) 1422-1435.